Fluorescent wavefront shaping using incoherent iterative phase conjugation

Dror Aizik[1,*], Ioannis Gkioulekas[2], and Anat Levin[1]

[1] *Department of Electrical and Computer Engineering, Technion, Haifa, Israel*
[2] *Robotics Institute, Carnegie Mellon University, PA, USA*
[*] *Corresponding author: droraizik@campus.technion.ac.il*

Compiled June 2, 2022

Wavefront shaping correction makes it possible to image fluorescent particles deep inside scattering tissue. This requires determining a correction mask to be placed in both excitation and emission paths. Standard approaches select correction masks by optimizing various image metrics, a process that requires capturing a prohibitively large number of images. To reduce acquisition cost, iterative phase conjugation techniques use the observation that the desired correction mask is an eigenvector of the tissue transmission operator. They then determine this eigenvector via optical implementations of the power iteration method, which require capturing orders of magnitude fewer images. Existing iterative phase conjugation techniques assume a linear model for the transmission of light through tissue, and thus only apply to fully-coherent imaging systems. We extend such techniques to the incoherent case for the first time. The fact that light emitted from different sources sums incoherently violates the linear model and makes linear transmission operators inapplicable. We show that, surprisingly, the non-linearity due to incoherent summation results in an order-of-magnitude acceleration in the convergence of the phase conjugation iteration.

http://dx.doi.org/10.1364/optica.XX.XXXXXX

1. INTRODUCTION

One of the core challenges when performing linear fluorescence microscopy inside tissue is the fact that biological tissue is highly scattering at visible wavelengths. This limits the clinical applicability of linear fluorescence microscopy techniques to thin superficial layers, as incoming and outgoing light propagating through the tissue is highly aberrated. In turn, this precludes widespread clinical use for tasks such as vasculature imaging, laser light therapy, and tumor detection.

A promising approach for overcoming the multiple scattering challenge is wavefront shaping correction: if one reshapes the incoming (or outgoing) coherent wavefront, such that its aberration is conjugate to the aberration that will happen inside the tissue, then after propagation the wavefront will focus into a sharp spot inside the tissue.

Adaptive optics techniques [1–3] were first used to correct modest aberrations, for example due to imperfect optics or refractive index variations in the tissue. More recently, wavefront shaping techniques [4, 5] have shown that it is possible to focus light through thick, highly-scattering layers [6–9]. Wavefront shaping ideas have found applications in a wide range of imaging modalities, including sound and light, coherent imaging and OCT, and incoherent fluorescence imaging using single-photon and multi-photon excitation. Our interest in this work is wavefront shaping for linear, single-photon fluorescence feedback.

The practical application of wavefront shaping is hindered by the difficulty of finding the wavefront correction to apply. This wavefront correction varies between different tissue layers, and even between different positions inside the same tissue sample. The simplest approach for finding the wavefront correction is to use a so-called guide star [10–19]: In this case, scattering arises from a strong *single* point source inside tissue, and a wavefront sensor [9, 14] directly measures the scattered wavefront.

Finding a wavefront shaping correction in the presence of multiple sources is more challenging, and typically involves optimization strategies relying on a variety of feedback mecha-

nisms [6–8, 11–13, 20–32]. This optimization is tractable when the wavefront correction can be described by a small number of parameters (e.g., using Zernike polynomials [33, 34]). However, to focus inside thick highly-scattering media, it is desired to use all the degrees of freedom of a modern spatial light modulator (SLM), often in the megapixel range. This is posing non-trivial optimization challenges [6, 12, 30, 35]. Even if we can test every such free parameter only once [32], the very large number of images captured for optimization limits any real-time applicability.

For fully coherent imaging systems, an alternative class of techniques estimating the wavefront correction is *iterative phase conjugation*. These techniques use the observation that a wavefront shaping correction focusing on a single point inside tissue is an *eigenvector* of the transmission matrix of the scattering sample [36]. They then find these eigenvectors using an optical implementation of the power method [37], which iterates between sending in a wavefront, measuring the scattered wavefront, and using the measurement as the successive input. Often this procedure converges after a very small number of iterations, leading to an order-of-magnitude acquisition speedup compared to standard optimization approaches. Iterative phase conjugation has found successful applications for sound [38, 39] and acousto-optics [40, 41], where the propagation is fully coherent. Although not presented this way, a similar iterative scheme was also applied for two-photon fluorescent imaging [42].

An important assumption underlying the coherent iterative phase conjugation scheme is that light scatters only once. This greatly limits its applicability to thin or sparse volumes. Our goal in this work is to develop an iterative phase conjugation approach that is applicable to linear (single-photon) fluorescent imaging. As the emitted light does not excite the tissue or the particles again, by working with fluorescent sources we can greatly relax the single scattering assumption, making our approach applicable to much thicker volumes, in particular tissue.

The primary technical challenge in this setting is that any uncorrected incident wavefront (such as the wavefronts used during the power method) will excite more than one fluorescing point inside the tissue sample, and the excited points will emit light that sums *incoherently*. Consequently, we cannot model the relation between input excitation and output fluorescent emission using a linear transmission operator, as fully-coherent iterative phase conjugation techniques do. To overcome this challenge, we analyze the incoherent case, and report two findings: First, we show that the same power method procedure as in the fully-coherent case can be used to recover the correction pattern also in the incoherent case. Second, we show that, whereas for the fully-coherent case the power method converges at an exponential rate, for the incoherent case it converges at a *doubly-exponential* rate. We demonstrate these findings experimentally, focusing light on fluorescent beads attached at the back of chicken breast tissue layers. Our technique achieves wavefront correction after capturing as few as $10-30$ images, compared to thousands of images captured by existing optimization-based wavefront shaping strategies for fluorescent imaging [21].

2. PRINCIPLE

Fig. 1 shows our imaging setup. A laser beam illuminates a tissue sample via a microscope objective. A phase SLM at the Fourier plane of the illumination arm modulates the illumination pattern. The modulated laser light excites fluorescent beads at the back of the sample. The emitted light is collected via the same objective, and reflected at a dichroic beam-splitter. A second phase SLM at the Fourier plane of the imaging arm modulates the emitted light. Lastly, the modulated light is measured by the front camera, which captures the images used by our algorithm. The setup includes a second validation camera behind the tissue sample. In our experiments we attached fluorescent beads at the back of the tissue layer, so that the validation camera can image them directly. We emphasize that measurements from this camera are *not* used by our algorithm, and that we only use the camera for validation purposes, to assess focusing quality and to image an undistorted reference of the bead layout.

We derive a strategy for efficiently finding a wavefront shaping modulation pattern for the illumination arm, allowing us to focus all light into a single spot inside the tissue sample. Once we have found the modulation pattern, we use the same modulation to also correct the emitted light in the imaging arm. This is possible because, in our linear fluorescent imaging setting, emission and excitation wavelengths are relatively close. Our approach extends to the incoherent imaging case iterative phase conjugation ideas that were previously used with coherent illumination. We begin our presentation by reviewing the coherent case, and then introduce the incoherent one.

Coherent iterative phase conjugation. Consider a set of K scattering (non fluorescent) particles inside a sample, and denote their positions by $\mathbf{o}_1,\ldots,\mathbf{o}_K$. We denote by $\mathbf{u}$ the value of an incoming 2D electric field at the input plane, and by $\boldsymbol{\nu}$ a $K\times 1$ vector of the field propagating through the sample at each of the K scatterers. Although $\mathbf{u}$ is a 2D field, we reshape it as a 1D vector and relate $\boldsymbol{\nu}$ to $\mathbf{u}$ as $\boldsymbol{\nu}=\boldsymbol{\mathcal{T}}^i\mathbf{u}$, where $\boldsymbol{\mathcal{T}}^i$ is the incoming transmission matrix describing coherent light propagation. $\boldsymbol{\mathcal{T}}^i$ is specific to the tissue sample being tested. Likewise, we denote by $\boldsymbol{\mathcal{T}}^o$ the back-propagation transmission matrix, describing the light returning from the particles to the sensor. The propagation of light to the particles and back to the sensor is then modeled using the *combined transmission matrix*

$$\boldsymbol{\mathcal{T}}^a \equiv \boldsymbol{\mathcal{T}}^o\cdot\boldsymbol{\mathcal{T}}^i. \tag{1}$$

Note that Eq. (1) offers a simplistic description of light propagation, assuming there is not much light back-scattered from other structures in the medium apart of the listed particles $\mathbf{o}_1,\ldots,\mathbf{o}_K$, and multiple scattering between the particles is negligible.

Under fully coherent illumination, the input illumination and the measured speckle intensity are related as

$$I=|\boldsymbol{\mathcal{T}}^a\mathbf{u}|^2. \tag{2}$$

Our goal is to find an illumination pattern $\mathbf{u}$ that will focus on one of the particles, so that $\boldsymbol{\nu}$ is a *one-hot vector*—non-zero only at a single point $\mathbf{o}_k$ for some k value. We note that focusing at any of the particles is sufficient for our setting; below, we show that once we focus at one point, we can use the memory effect to focus at nearby ones.

To find a wavefront modulation we need access to $\boldsymbol{\mathcal{T}}^i$, but in practice we can only measure $\boldsymbol{\mathcal{T}}^a$. The wave conjugation principle states that the returning transmission matrix is the transpose of the incoming one, $\boldsymbol{\mathcal{T}}^o=\boldsymbol{\mathcal{T}}^{i\top}$ [43]. With this assumption, consider an illumination field $\mathbf{u}$ that, after propagating through the tissue sample, generates a one-hot $\boldsymbol{\nu}$ vector. If we focus all light at one particle, then by the wave conjugation principle the returning field is proportional to the incoming one. Therefore, we can express the returning intensity in Eq. (2) as

$$I=s|\mathbf{u}|^2=|\boldsymbol{\mathcal{T}}^a\mathbf{u}|^2, \tag{3}$$

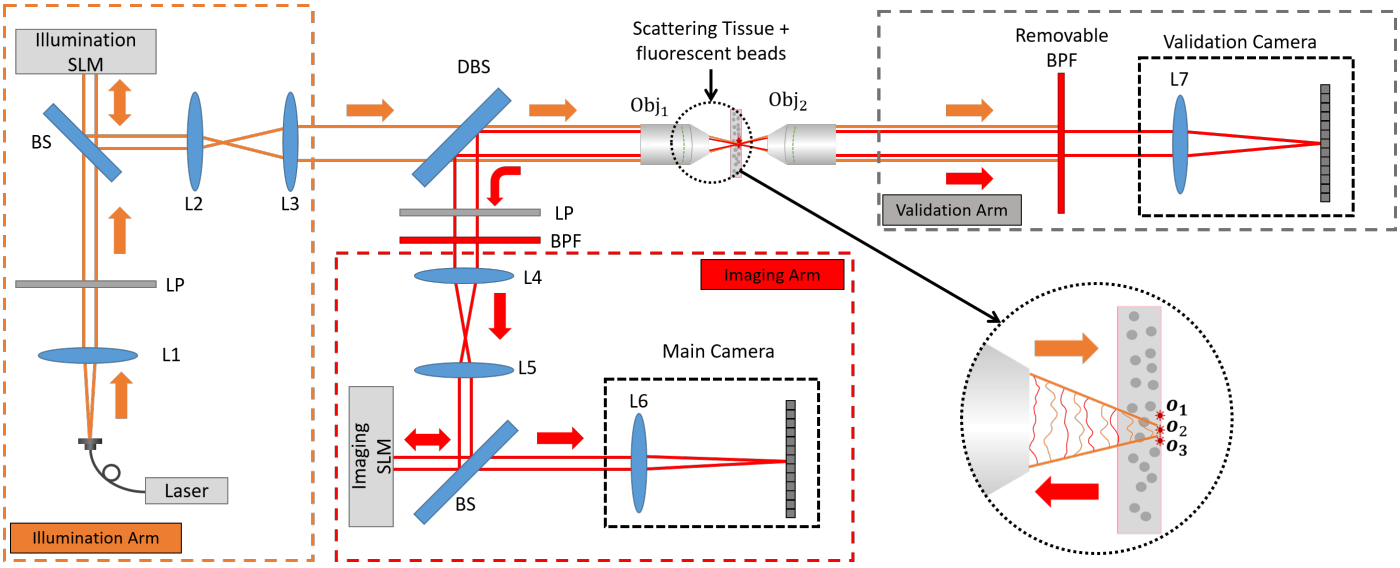

Fig. 1. Our wavefront correction fluorescent microscope setup: A laser beam is exciting fluorescent beads at the back of a tissue layer, and fluorescent emission is scattered again through the tissue, reflects at a dichroic beam-splitter and is collected by a main (front) camera. We place two SLMs in the Fourier planes of both illumination and imaging arms to allow reshaping these wavefronts. A validation camera views the beads at the back of the tissue directly. This camera is not actually used by the algorithm, and is only assessing its success. LP=linear polarizer, BS=beam-splitter, DBS=dichroic beam-splitter, BPF=bandpass filter, $L1 \dots L7$=lenses, Obj=Objective.

where s is a scale factor. That is, a focusing wavefront is an *eigenvector* of the combined transmission matrix $\boldsymbol{\mathcal{T}}^a$. Consequently, if we can compute eigenvectors efficiently, we can find a wavefront that focuses all the light in a single spot.

A common class of numerical algorithms for computing matrix eigenvectors follows the *power method* [37]. This algorithm relies on the fact that the sequence $\mathbf{u}, \boldsymbol{\mathcal{T}}^a\mathbf{u}, (\boldsymbol{\mathcal{T}}^a)^2\mathbf{u}, (\boldsymbol{\mathcal{T}}^a)^3\mathbf{u} \dots$ converges exponentially-fast to the largest eigenvector of $\boldsymbol{\mathcal{T}}^a$. Iterative phase conjugation algorithms [38–41] do not acquire the full transmission matrix $\boldsymbol{\mathcal{T}}^a$, but instead directly measure its optical operation on wavefronts of interest. They begin by illuminating the sample with a random wavefront $\mathbf{u}^0$, then iteratively measure the resulting output wavefront, and use its conjugate as a successive illumination pattern. That is, at the t-th iteration, the incident wavefront is $\mathbf{u}^{(t)} = (\boldsymbol{\mathcal{T}}^a\mathbf{u}^{(t-1)})^*$, where * denotes complex conjugation. When measuring intensity images $I = |\boldsymbol{\mathcal{T}}^a\mathbf{u}^{(t)}|^2$, computing $\mathbf{u}^{(t+1)}$ also requires estimating the phase of the measured intensity pattern.

Using the exponential convergence property of the power method it can be shown [37], and we review the derivation in the supplement, that the energy focused on the k-th particle at the t-th iteration follows a geometric sequence of the form

$$|\boldsymbol{\nu}_k^{(t)}| = \frac{1}{N_t}\lambda_k^t \cdot c_k, \tag{4}$$

for constants λ_k, c_k and a normalization factor $N_{(t)}$ we derive in the supplement. Eq. (4) implies that the energy at the k-th particle scales exponentially with the iteration number t. Thus, each iteration increases the gap in energy between the strongest and second strongest particles, and the sequence quickly converges to a one-hot $\boldsymbol{\nu}$ vector.

Incoherent phase conjugation. The main limitation of coherent iterative phase conjugation is that to describe the propagation using the model of Eq. (1) one neglects multiple scattering between the particles, as well as back-scattering from any other tissue components. This in turn limits the applicability of the technique to thin or sparse volumes. By using fluorescent emission we remove this restriction, because even in thick tissue it is reasonable to assume that the emitted light does not excite the tissue or the other beads again. Moreover, we show that the incoherent summation of fluorescent emission results in largely accelerated convergence. However, an adaptation of the power method to the incoherent case is not straightforward due to the non-linearity imposed by incoherent emission.

To study the incoherent case we need to adjust the above model in two ways. First, we now mark by $\mathbf{o}_1, \dots, \mathbf{o}_K$ the positions of the fluorescent particles rather than all scatterers in the volume. We use $\boldsymbol{\mathcal{T}}^i$ to describe propagation at the excitation wavelength λ_i, and $\boldsymbol{\mathcal{T}}^o$ to describe propagation at the emission wavelength λ_o. Despite the small difference between emission and excitation wavelengths, we still assume that $\boldsymbol{\mathcal{T}}^o \approx \boldsymbol{\mathcal{T}}^{i\top}$. Note that $\boldsymbol{\mathcal{T}}^i, \boldsymbol{\mathcal{T}}^o$ describe multiple scattering events by other tissue components apart of the listed fluorescent particles $\mathbf{o}_1, \dots, \mathbf{o}_K$.

Second, whereas in the coherent case the output wavefront is a linear function of the input, $\boldsymbol{\mathcal{T}}^a\mathbf{u}^{(t)}$, this linear model no longer holds when incoherently summing light from different emitters. To derive an image formation model for this case, we again use $\boldsymbol{\nu} = \boldsymbol{\mathcal{T}}^i\mathbf{u}$ to denote the field arriving at the fluorescent emitters. Fluorescent emission is proportional to the intensity of $\boldsymbol{\nu}$, and the recorded intensity equals an incoherent summation

$$I = \sum_k |\boldsymbol{\mathcal{T}}^o_{:,k}|^2 |\boldsymbol{\nu}_k|^2, \tag{5}$$

where $\boldsymbol{\mathcal{T}}^o_{:,k}$ is the k-th column of $\boldsymbol{\mathcal{T}}^o$.

If we manage to focus and $\boldsymbol{\nu}$ is a one-hot vector, then there is only a single non zero term in the summation of Eq. (5). Denoting the index of this non zero entry by k_o we can express the

intensity in Eq. (5) as

$$I = |\mathcal{T}^o_{:,k_o}|^2 |\nu_{k_o}|^2 = |\mathcal{T}^o_{:,k_o}\nu_{k_o}|^2 = |\mathcal{T}^o\nu|^2 = \\ = |\mathcal{T}^o\mathcal{T}^i\mathbf{u}|^2 = |\mathcal{T}^a\mathbf{u}|^2. \quad (6)$$

So effectively, when focusing is achieved, Eq. (5) reduces to Eq. (2), and the measured intensity is equivalent to $|\mathcal{T}^a\mathbf{u}|^2$. Therefore in the incoherent case, a focusing wavefront is still an eigenvector of the transmission operator $\mathcal{T}^a = \mathcal{T}^o \cdot \mathcal{T}^i$.

Motivated by this observation we apply iterative phase conjugation as in the coherent case. As we measure only the intensity of the emitted light, to recover the phase of the wavefront, we use a phase diversity acquisition scheme [44]. We place $J = 5$ known modulation patterns H^j on the phase SLM of the imaging arm. At the t-th iteration, we measure speckle intensity images

$$I^{(t,j)} = \sum_k |h^j \star \mathcal{T}^o_{:,k}|^2 |\nu^{(t)}_k|^2, \quad (7)$$

where $\star$ is convolution, h^j is the Fourier transform of the pattern we placed on the SLM, and $|\nu^t_k|^2$ is the intensity arriving at the k-th particle in the t-th iteration. We use gradient descent optimization to find a complex wavefront $\mathbf{u}^{(t+1)}$ minimizing

$$\sum_j \left| I^{(t,j)} - |h^j \star \mathbf{u}^{(t+1)}|^2 \right|^2. \quad (8)$$

We then use the conjugate of the estimated wavefront as the excitation of the next iteration, and display it on the SLM of the illumination arm.

When the intensity image is an incoherent summation from multiple sources there is typically no wavefront minimizing Eq. (8) with zero error. Despite this, we show in the supplement that the resulting wavefront is approximately equal to a weighted linear combination of the wavefronts $\mathcal{T}^o_{:,k}$ generated by the individual sources. Sources with stronger emission receive a higher weight in the reconstruction, which further increases their weight in the next iteration of the algorithm.

In the supplement, we analyze the differences between the coherent and incoherent models, and we show that the incoherent summation results in an asymptotically faster convergence rate. In particular, we prove the following claim.

Claim 1. *The convergence of the power iterations in the incoherent case follows a doubly exponential sequence of the form*

$$|\nu^{(t)}_k|^2 = \frac{1}{N_{(t)}} (\lambda_k)^{2^t} \cdot c_k \quad (9)$$

for scalars λ_k, c_k derived in the supplement.

To understand the difference, we note that in the coherent case of Eq. (4), the energy at the different particles scales as λ^t_k. In the incoherent case, we get another exponential factor, and energy scales as $(\lambda_k)^{2^t}$. Intuitively, this is because the fluorescent emission is proportional to the intensity of the field $|\nu^{(t)}|^2$ arriving at the particles, rather than to the field $\nu^{(t)}$ itself. As $\nu^{(t)}$ is squared *in every iteration*, the squaring is accumulated into another exponential term.

To visualize the faster convergence, in Fig. 2 we simulated coherent and incoherent power iterations on a random transmission matrix sampled as described in supplement.

In practice, in the hardware implementation described below, our algorithm converged within about $2-6$ iterations. Accounting for the 5 images used for phase acquisition at each step, our approach can find a wavefront correction pattern using about $10-30$ image measurements. This provides orders of magnitude speedup compared to recent optimization-based approaches recovering a wavefront shaping correction pattern using a single-photon fluorescent feedback, which requires capturing thousands of images [21].

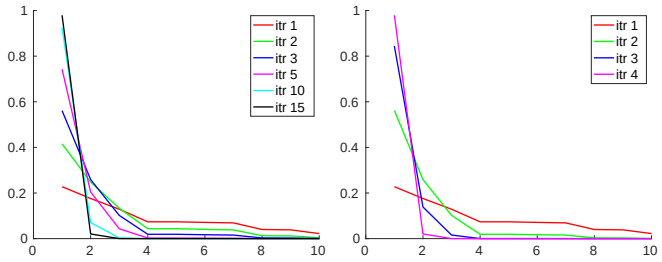

(a) Coherent (b) Incoherent

Fig. 2. Simulating coherent and incoherent convergence: We plot the power of scatterers $|\nu^{(t)}_k|^2$, for different iterations of the iterative phase conjugation algorithm. As predicted by theory, the incoherent case converges into a one-hot vector within a smaller number of iterations (compare 4 incoherent iterations to 15 coherent ones). The x axis of our plot corresponds to scatterer index k, where for ease of visualization we sort these in decreasing order of power.

3. RESULTS

In our experimental implementation, we use fluorescent microspheres of diameter 200 nm (ThermoFisher FluoSpheres dark red), excited and imaged with $NA = 0.5$ objectives so that the particles are slightly smaller than the diffraction limit. For excitation, we use a 637 nm laser, and to measure emission we use a band-pass filter of center wavelength 680 nm and bandwidth 10 nm. In the main paper, we use as scattering samples chicken breast tissue slices of thickness $200-400\mu m$. In the supplement, we also show results using other scattering phantoms, including parafilm and polystyrene beads dispersed in agarose. For all examples, significant scattering is present, and a standard microscope cannot image the actual source pattern. The beads are attached at the back of the tissue layer, separated only by a $150\mu m$ microscope cover glass. We use two Pluto Holoeye SLMs, and a Prime BSI sCMOS sensor for imaging fluorescent emission.

Fig. 3 visualizes the power iterations of our algorithm from both the main camera and the validation camera. In the beginning the main camera sees a wide speckle pattern, and from the validation camera we can see that a wide speckle pattern reaches the back of the tissue. We also use a band-pass filter on the validation camera to image the beads excited by each modulation pattern. The validation camera confirms that as the algorithm proceeds the illumination reaching the back of the tissue converges into a single spot. Even if we manage to excite a single bead, the emitted light can scatter on its way to the main camera and generate a speckle pattern. In Fig. 3 we first visualize this scattering by showing the views of the main camera when modulation is used in the illumination SLM to focus the excitation, but with no modulation at the imaging arm. In addition, we show what happens if the modulation pattern of each iteration is also placed on the SLM of the imaging arm. As the iterations proceed and the modulation pattern improves, the imaging SLM refocuses the light emitted from the excited bead

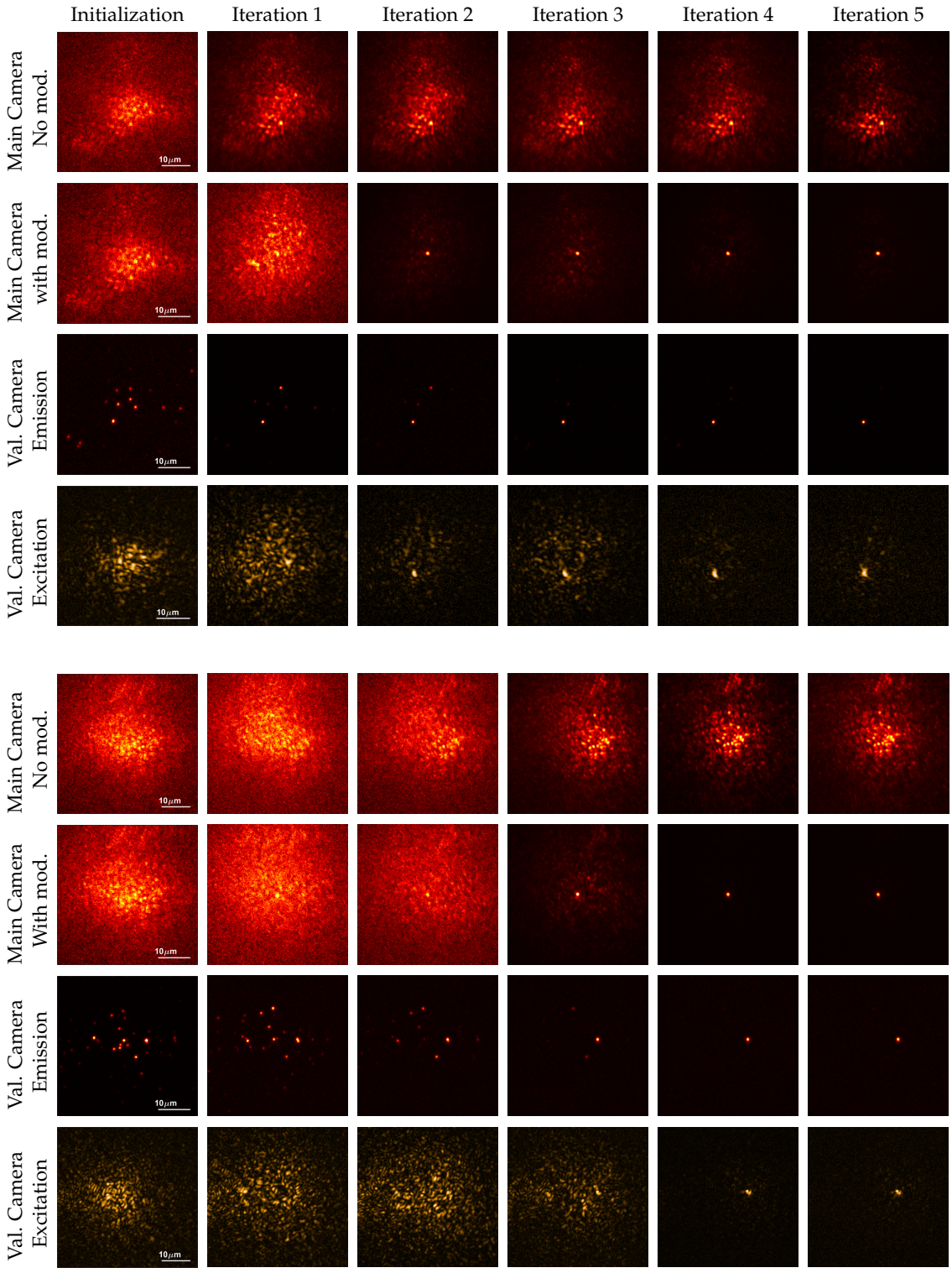

Fig. 3. Algorithm convergence. We show the iterations of our power algorithm on two different tissue samples. We demonstrate views via the main camera seeing the front of the tissue with and without the modulation correction, and the validation camera observing fluorescent beads directly. To better appreciate the focusing we used the validation camera to capture both the excitation and emission wavelengths. In the first iteration we see a speckle image, but as power iterations proceed the illumination wavefront converges and focuses on a single bead. When the same modulation pattern is placed at the imaging arm, imaging aberrations are corrected and one can see a sharp image of the excited bead. Note that images in different iterations have very different ranges, and for better visualization each image was normalized to its own maximum.

into a single sensor spot.

When multiple fluorescing particles are present in the field of view, the algorithm typically converges to the strongest one. However the particle at which the algorithm converges may

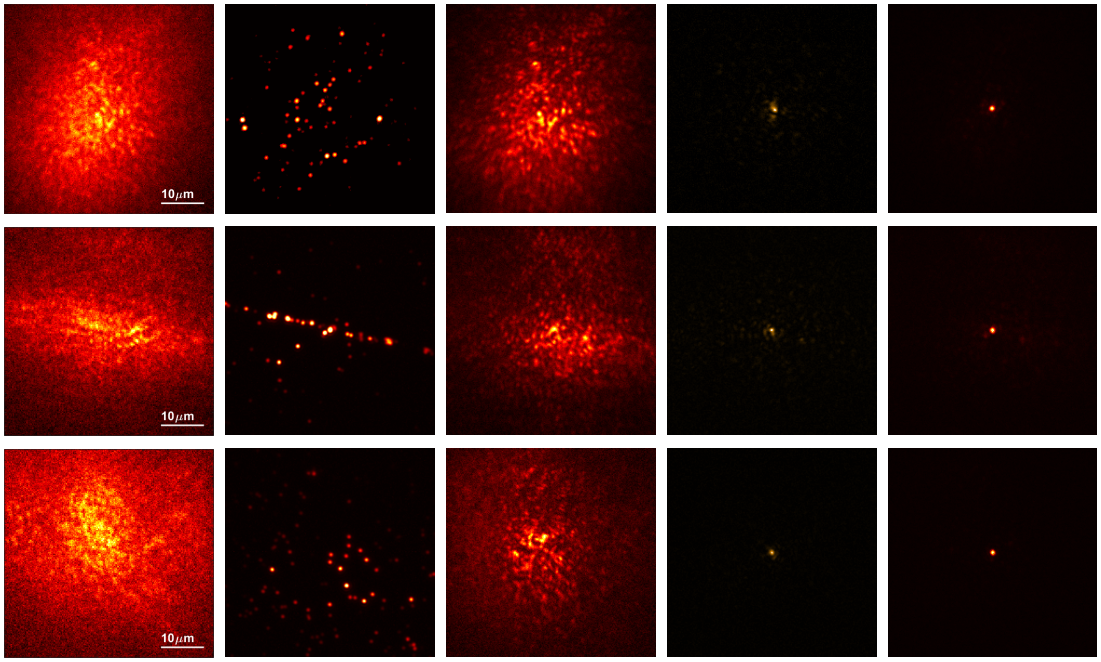

(a) Initial speckle (b) Wide illum. validation camera (c) Speckle from single source (d) Focused illum valid. camera (e) Focused illum+ corrected emission

Fig. 4. Analyzing focusing inside tissue. each row visualizes a different experiment on a different tissue slice. (a) Main camera when SLMs are blank, demonstrating initial speckles. (b) Validation camera when illumination SLM is blank, demonstrating the enlightened bead layout at emission wavelength. (c) Speckles from one bead (imaging SLM is blank and illumination SLM is corrected), demonstrating the amount of aberration. (d) Validation camera when illumination is corrected, demonstrating that most light gets into a single spot (excitation wavelength). (e) Main camera when both SLMs are corrected, demonstrating focusing in a single spot.

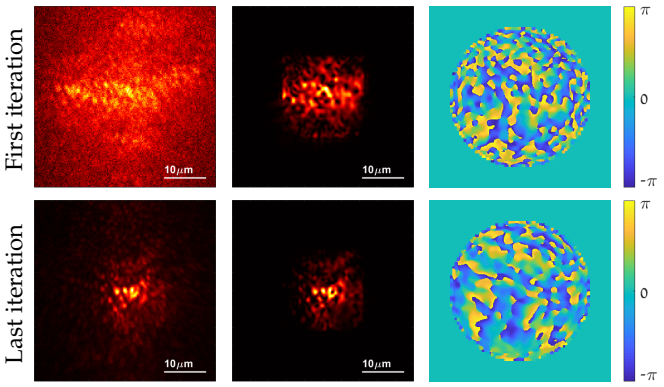

(a) Speckle image (b) Recovered intensity Sensor plane (c) Recovered phase Fourier plane

Fig. 5. Phase reconstruction: (a) Speckle image captured by the main camera in the first and last iteration of the algorithm. (b) The intensity of the recovered aberration correction in the sensor plane. In the first iteration when multiple incoherent beads are excited we cannot fully explain the image as a single coherent wavefront. But as the algorithm converges to excite a single bead the recovered wavefront better matches with the captured image. (c) The phase of the recovered aberration correction in the Fourier plane, which is the mask presented on the SLM.

vary due to multiple reasons such as imaging noise, fluorescence bleaching or local minima of the phase diversity optimization. Convergence can also change if the optimization is initialized with a different speckle pattern.

In Fig. 4 we demonstrate the final iteration of our algorithm on a few additional examples. In Fig. 4(c) we also visualize the actual scattering of the tissue layer. To this end we place the correction mask on the illumination SLM only, bringing all light to excite a single bead. We use no correction on the imaging arm, allowing us to visualize the speckles from this source. This image corresponds to a column of the transmission matrix $\mathcal{T}^o$.

In Fig. 5, we visualize the phase diversity acquisition results at the first and last iterations of the algorithm. Fig. 5(a) shows the image from the main camera in both iterations when the imaging SLM applies no correction. Fig. 5(b) shows the intensity of the recovered wavefront at the plane of the camera sensor, which is set conjugate to the plane of the fluorescent sources. The phase diversity optimization attempts to explain the images in Fig. 5(a). However, in the first iteration, the captured speckle image is an incoherent summation from multiple particles, which the optimization objective of Eq. (8) attempts to explain with a single coherent wavefront; thus the result is imperfect. In the last iteration, the algorithm excites a single particle, and indeed the estimated wavefront better explains the captured intensity. Finally, Fig. 5(c) shows the retrieved phase in the frequency domain, which is essentially the pattern displayed on the SLM. We note that, as we use a phase-only SLM, we effectively correct only the phase of the wavefront and neglect its amplitude.

Imaging a wide field of view. The recovered modulation pattern is designed to focus at a single particle inside the tissue sample. However, due to the memory effect, the corrections of nearby spots are similar. We demonstrate this experimentally in the second row of Fig. 6: We place a random pattern on the illumination arm, which results in exciting multiple fluorescing particles. We then place the correction pattern recovered for focusing on one

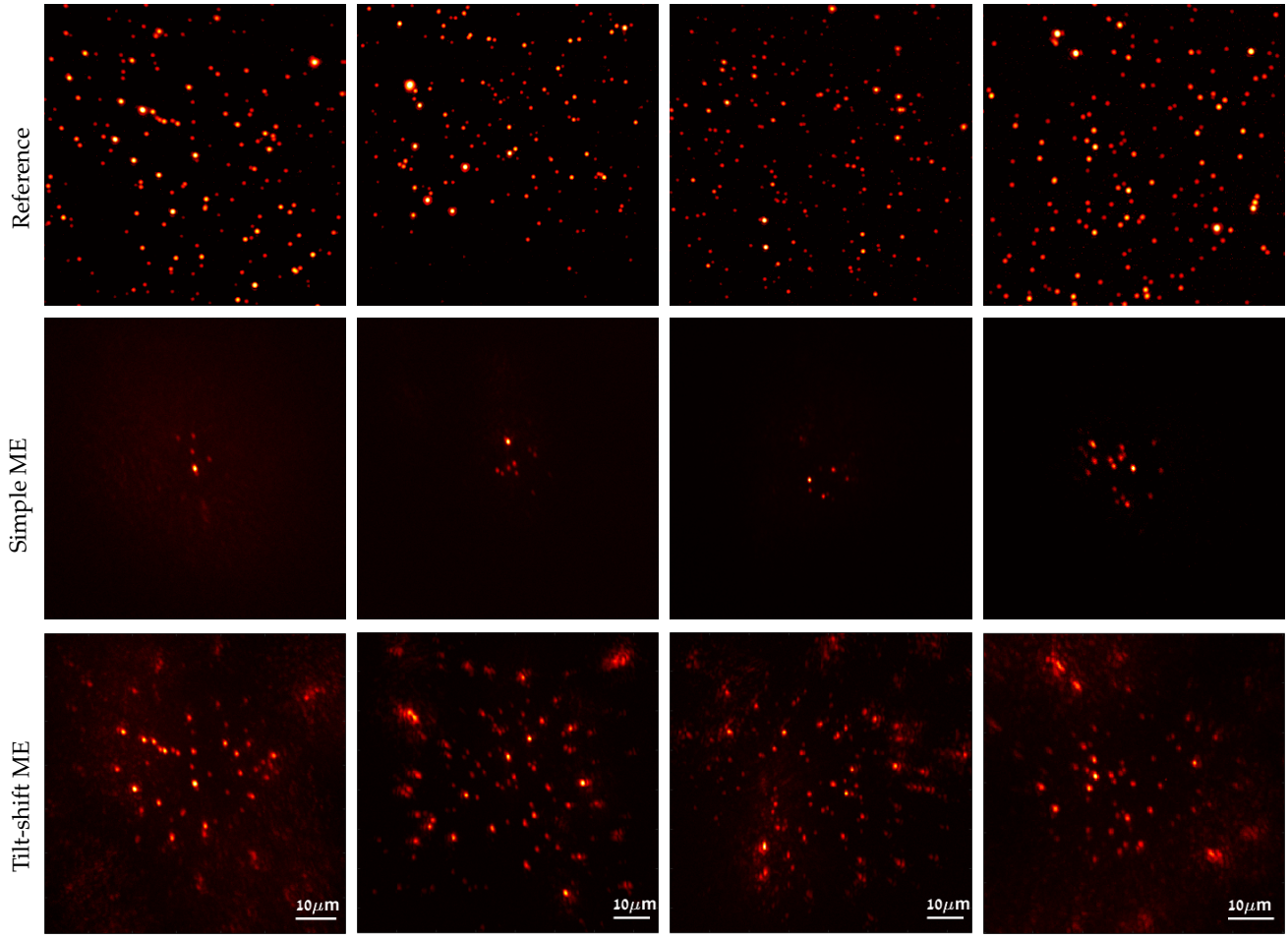

Fig. 6. Imaging a wide area of fluorescent sources, behind 4 different tissue slices. Top: Reference image from validation camera. Second row: Imaging fluorescent sources within a small region behind the tissue using a simplified memory effect. We use the correction mask on the imaging arm, and use wide illumination to excite multiple beads. Third row: Using the tilt-shift memory effect to image a wider area, by shifting the imaging mask in the Fourier plane.

of the fluorescing particles on the imaging arm. We observe that, thanks to the memory effect, the camera can image a small neighborhood of particles around the focus points, and not just the single particle the correction pattern corresponds to. To further improve on this, we use the tilt-shift memory effect [45, 46] and shift the modulation mask in the Fourier plane. As we explain in the supplement, this shift allows us to focus at nearby regions using the same correction pattern. In the third row of Fig. 6, we image a wider range of particles behind the tissue sample, by scanning 21×21 such shifts. We acknowledge that by placing the SLM at a plane conjugate to the sample itself [45, 47] rather than in the Fourier plane, we can probably expand the region corrected by a single modulation and reduce the number of required shifts. Even after exploiting the tilt-shift, the extent of the memory effect is limited, and beads at the periphery of the images of the last row in Fig. 6 are either not recovered or strongly aberrated. Imaging beyond this region would require applying another set of power iterations to calibrate a different wavefront modulation, amplifying the importance of the faster convergence of our proposed procedure.

4. DISCUSSION

We extended iterative phase conjugation algorithms to apply to incoherent fluorescent imaging. Even though the incoherent contribution of different sources alters the linear transmission model from which these algorithms are derived, we show that the non-linear incoherent model accelerates convergence rate, from exponential to doubly-exponential. To find a wavefront correction pattern, we need to excite the tissue with a very small number of trial patterns and measure the resulting excitation. The number of measurements is orders of magnitude smaller than that of previous optimization-based techniques.

We used the recovered modulation pattern to image fluorescent particles placed behind a tissue sample. However, wavefront correction in thick tissue is spatially-varying, and each modulation pattern is only usable for imaging a limited region, with size determined by the memory effect. To image a wider region behind the tissue sample, we have to apply the modulation recovery algorithm multiple times in different sub-regions. This makes it even more important to have fast wavefront shaping algorithms. One way to further reduce the number of acquired images is to use a tilt-shift adaptation of the aberration correction estimated in one region, and initialize with it the power iteration in neighboring sub-regions.

Our current results apply only on a sparse set of fluorescent particles. Increasing the density of the sources is challenging because as speckle contrast decays [48], it is harder for the phase diversity acquisition scheme to recover phase. To alleviate this problem, we could adopt other phase acquisition schemes, such as using a Shack-Hartmann sensor [49].

Another issue which may challenge convergence with a dense continuous fluorescent object is two nearby spots emitting similar power. This is due to the fact that when a transmission matrix contains multiple eigenvectors with the same eigenvalue, power iterations may not separate them, and can converge to a linear combination of the two eigenvectors. We note however that the incoherent convergence rate as analyzed in supplement Eq. (26) depends not only on the actual eigenvalues, but also on the initial excitation $\mathcal{T}^{i}_{k,:}\mathbf{u}^{(0)}$. As this excitation is usually a highly varying speckle pattern, there is a better chance to separate between nearby illuminators of similar power.

Our approach also relies on the assumption that the excitation and emission wavelength are close enough so that the excitation and emission transmission matrices are sufficiently similar. Also, as the emitted light contains multiple wavelengths, these can produce somewhat different speckle patterns. There is evidence in the literature that speckle patterns produced by nearby wavelengths are correlated [50], but this similarity degrades as the tissue sample thickness increases [51]. In our experimental implementation, there is a 40 nm gap between the emission and excitation wavelengths. In linear fluorescence imaging, the gap between excitation to emission can be made lower than that, leading to even stronger correlation between the wavefronts.

Relationship to memory-effect techniques. Our work is orthogonal to approaches for imaging fluorescent sources through tissue using speckle statistics, and in particular the memory effect [48, 52, 53]. Recently, such approaches were successful in imaging a sparse set of fluorescent particles inside tissue, using hundreds [22, 54] or even just dozens [55] of images. While the field of view of a wavefront shaping modulation is constrained by the extent of the memory effect, as demonstrated in Fig. 6, approaches based on the memory effect can recover full-frame patterns with much wider field of view. By contrast, memory effect correlations only exist in thin tissue layers, while approaches based on phase conjugation can theoretically achieve larger penetration depths. However, in practice, the penetration depth is greatly constrained by the very weak signal-to-noise ratio of fluorescent emission. Approaches based on phase conjugation make it possible to not only *image* through scattering, but also *focus light* inside scattering tissue, a capability that memory effect approaches lack. Focusing inside tissue is important for applications such as laser treatment therapy, confocal microscopy, and STED microscopy. Finally, a modulation recovered from fluorescent sources can also be used to image adjacent non-fluorescent tissue structures.

Acknowledgments

We thank Lucien Weiss and Onit Alalouf for their help preparing experimental data.

Disclosure

The authors declare no conflicts of interest.

Data availability

Data underlying the results presented in this paper are available in Ref. [56]

REFERENCES

1. M. Booth, "Adaptive optical microscopy: The ongoing quest for a perfect image," Light. Sci. Appl. **3**, e165 (2014).
2. N. Ji, "Adaptive optical fluorescence microscopy," Nat. Methods **14**, 374–380 (2017).
3. K. Hampson, R. Turcotte, D. Miller, K. Kurokawa, J. Males, N. Ji, and M. Booth, "Adaptive optics for high-resolution imaging," Nat. Rev. Methods Primers **1**, 68 (2021).
4. H. Yu, J. Park, K. Lee, J. Yoon, K. Kim, S. Lee, and Y. Park, "Recent advances in wavefront shaping techniques for biomedical applications," Curr. Appl. Phys. **15**, 632–641 (2015).
5. S. Gigan, O. Katz *et al.*, "Roadmap on wavefront shaping and deep imaging in complex media," arXiv preprint arXiv:2111.14908 (2021).
6. I. M. Vellekoop and A. P. Mosk, "Focusing coherent light through opaque strongly scattering media," Opt. Lett. (2007).
7. Z. Yaqoob, D. Psaltis, M. Feld, and C. Yang, "Optical phase conjugation for turbidity suppression in biological samples," Nat. photonics (2008).
8. I. M. Vellekoop, A. Lagendijk, and A. P. Mosk, "Exploiting disorder for perfect focusing," Nat. Photonics (2010).
9. I. M. Vellekoop, M. Cui, and C. Yang, "Digital optical phase conjugation of fluorescence in turbid tissue," Appl. Phys. Lett. (2012).
10. R. Horstmeyer, H. Ruan, and C. Yang, "Guidestar-assisted wavefront-shaping methods for focusing light into biological tissue," Nat. Photonics (2015).
11. J. Tang, R. N. Germain, and M. Cui, "Superpenetration optical microscopy by iterative multiphoton adaptive compensation technique," Proc. Natl. Acad. Sci. **109**, 8434–8439 (2012).
12. O. Katz, E. Small, Y. Guan, and Y. Silberberg, "Noninvasive nonlinear focusing and imaging through strongly scattering turbid layers," Optica. **1**, 170–174 (2014).
13. C. Wang, R. Liu, D. Milkie, W. Sun, Z. Tan, A. Kerlin, T.-W. Chen, D. Kim, and N. Ji, "Multiplexed aberration measurement for deep tissue imaging in vivo," Nat. methods **11** (2014).
14. T.-L. Liu *et al.*, "Observing the cell in its native state: Imaging subcellular dynamics in multicellular organisms," Science **360** (2018).
15. R. Fiolka, K. Si, and M. Cui, "Complex wavefront corrections for deep tissue focusing using low coherence backscattered light," Opt. Express **20**, 16532–16543 (2012).
16. J. Jang, J. Lim, H. Yu, H. Choi, J. Ha, J.-H. Park, W.-Y. Oh, W. Jang, S. Lee, and Y. Park, "Complex wavefront shaping for optimal depth-selective focusing in optical coherence tomography," Opt. Express **21**, 2890–2902 (2013).
17. X. Xu, H. Liu, and L. Wang, "Time-reversed ultrasonically encoded optical focusing into scattering media," Nat. Photonics **5**, 154–157 (2011).
18. Y. M. Wang, B. Judkewitz, C. A. DiMarzio, and C. Yang, "Deep-tissue focal fluorescence imaging with digitally time-reversed ultrasound-encoded light," Nat. Commun. **3** (2012).
19. F. Kong, R. H. Silverman, L. Liu, P. V. Chitnis, K. K. Lee, and Y. C. Chen, "Photoacoustic-guided convergence of light through optically diffusive media," Opt. Lett. **36**, 2053–2055 (2011).
20. J. Li, D. R. Beaulieu, H. Paudel, R. Barankov, T. G. Bifano,

and J. Mertz, "Conjugate adaptive optics in widefield microscopy with an extended-source wavefront sensor," Optica. **2**, 682–688 (2015).
21. A. Boniface, B. Blochet, J. Dong, and S. Gigan, "Noninvasive light focusing in scattering media using speckle variance optimization," Optica. (2019).
22. A. Boniface, J. Dong, and S. Gigan, "Non-invasive focusing and imaging in scattering media with a fluorescence-based transmission matrix," Nat. Commun. (2020).
23. S. Bonora and R. J. Zawadzki, "Wavefront sensorless modal deformable mirror correction in adaptive optics: optical coherence tomography," Opt. Lett. **38**, 4801–4804 (2013).
24. J. Antonello, A. Barbotin, E. Z. Chong, J. Rittscher, and M. J. Booth, "Multi-scale sensorless adaptive optics: application to stimulated emission depletion microscopy," Opt. Express **28**, 16749–16763 (2020).
25. T. Yeminy and O. Katz, "Guidestar-free image-guided wavefront-shaping," Sci. Adv. **7**, eabf5364 (2021).
26. G. Stern and O. Katz, "Noninvasive focusing through scattering layers using speckle correlations," Opt. Lett. (2019).
27. A. Daniel, D. Oron, and Y. Silberberg, "Light focusing through scattering media via linear fluorescence variance maximization, and its application for fluorescence imaging," Opt. Express (2019).
28. H. R. G. W. Verstraete, S. Wahls, J. Kalkman, and M. Verhaegen, "Model-based sensor-less wavefront aberration correction in optical coherence tomography," Opt. Lett. **40**, 5722–5725 (2015).
29. S. Kang, S. Jeong, W. Choi, H. Ko, T. Yang, J. Joo, J.-S. Lee, Y. Lim, Q. Park, and W. Choi, "Imaging deep within a scattering medium using collective accumulation of single-scattered waves," Nat. Photonics (2015).
30. D. B. Conkey, A. N. Brown, A. M. Caravaca-Aguirre, and R. Piestun, "Genetic algorithm optimization for focusing through turbid media in noisy environments," Opt. Express (2012).
31. S. M. Popoff, G. Lerosey, R. Carminati, M. Fink, A. C. Boccara, and S. Gigan, "Measuring the transmission matrix in optics: An approach to the study and control of light propagation in disordered media," Phys. Rev. Lett. (2010).
32. Y. Chen, M. K. Sharma, A. Sabharwal, A. Veeraraghavan, and A. C. Sankaranarayanan, "3PointTM: Faster measurement of high-dimensional transmission matrices," in *Euro. Conf. Computer Vision (ECCV)*, (2020).
33. M. J. Booth, M. A. A. Neil, R. Juškaitis, and T. Wilson, "Adaptive aberration correction in a confocal microscope," Proc. Natl. Acad. Sci. **99**, 5788–5792 (2002).
34. J.-H. Park, L. Kong, Y. Zhou, and M. Cui, "Large-field-of-view imaging by multi-pupil adaptive optics," Nat. methods **14** (2017).
35. S. M. Popoff, A. Aubry, G. Lerosey, M. Fink, A. C. Boccara, and S. Gigan, "Exploiting the time-reversal operator for adaptive optics, selective focusing, and scattering pattern analysis," Phys. Rev. Lett. **107**, 263901 (2011).
36. S. Popoff, A. Aubry, G. Lerosey, M. Fink, and S. Gigan, "Exploiting the time-reversal operator for adaptive optics, selective focusing, and scattering pattern analysis," Phys. review letters **107**, 263901 (2011).
37. L. N. Trefethen and D. Bau, *Numerical Linear Algebra* (SIAM, 1997).
38. C. Prada, J. Thomas, and M. Fink, "The iterative time reversal process: Analysis of the convergence," The J. Acoust. Soc. Am. **97**, 62–71 (1995).
39. H. C. Song, W. A. Kuperman, W. S. Hodgkiss, T. Akal, and C. Ferla, "Iterative time reversal in the ocean," The J. Acoust. Soc. Am. **105**, 3176–3184 (1999).
40. K. Si, R. Fiolka, and M. Cui, "Breaking the spatial resolution barrier via iterative sound-light interaction in deep tissue microscopy," Sci. reports **2**, 748 (2012).
41. H. Ruan, M. Jang, B. Judkewitz, and C. Yang, "Iterative time-reversed ultrasonically encoded light focusing in backscattering mode," Sci. reports **4**, 7156 (2014).
42. I. Papadopoulos, J.-S. Jouhanneau, J. Poulet, and B. Judkewitz, "Scattering compensation by focus scanning holographic aberration probing (f-sharp)," Nat. Photonics (2016).
43. S. Rotter and S. Gigan, "Light fields in complex media: Mesoscopic scattering meets wave control," Rev. Mod. Phys. (2017).
44. L. M. Mugnier, A. Blanc, and J. Idier, "Phase diversity: A technique for wave-front sensing and for diffraction-limited imaging," (Elsevier, 2006), pp. 1–76.
45. G. Osnabrugge, R. Horstmeyer, I. N. Papadopoulos, B. Judkewitz, and I. M. Vellekoop, "Generalized optical memory effect," Optica. (2017).
46. C. Bar, M. Alterman, I. Gkioulekas, and A. Levin, "Single scattering modeling of speckle correlation," in *ICCP*, (2021).
47. J. Mertz, H. Paudel, and T. G. Bifano, "Field of view advantage of conjugate adaptive optics in microscopy applications," Appl. Opt. (2015).
48. M. Alterman, C. Bar, I. Gkioulekas, and A. Levin, "Imaging with local speckle intensity correlations: theory and practice," ACM TOG (2021).
49. R. Shack, "Production and use of a lecticular hartmann screen," J. Opt. Soc. Am. **61**, 656–661 (1971).
50. L. Zhu, J. B. de Monvel, P. Berto, S. Brasselet, S. Gigan, and M. Guillon, "Chromato-axial memory effect through a forward-scattering slab," Optica. **7**, 338–345 (2020).
51. D. Andreoli, G. Volpe, S. Popoff, O. Katz, S. Grésillon, and S. Gigan, "Deterministic control of broadband light through a multiply scattering medium via the multispectral transmission matrix," Sci. Reports **5** (2015).
52. J. Bertolotti, E. G. van Putten, C. Blum, A. Lagendijk, W. L. Vos, and A. P. Mosk, "Non-invasive imaging through opaque scattering layers," (2012).
53. O. Katz, P. Heidmann, M. Fink, and S. Gigan, "Non-invasive single-shot imaging through scattering layers and around corners via speckle correlation," Nat. Photonics (2014).
54. L. Zhu, F. Soldevila, C. Moretti, A. d'Arco, A. Boniface, X. Shao, H. B. de Aguiar, and S. Gigan, "Large field-of-view non-invasive imaging through scattering layers using fluctuating random illumination," arXiv preprint arXiv:2017.08158 (2021).
55. W. Chen, A. Levin, M. O'Toole, and A. Sankaranarayanan, "Enhancing speckle statistics for imaging inside scattering media," arXiv preprint (2022).
56. D. Aizik, "Data for power iterations algorithm," https://github.com/droraizik/Data_waveshaping_eigenvectors (2022).